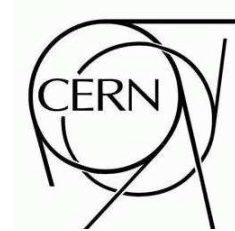


ATLAS NOTE

August 27, 2008



CSC NOTE - PHOTON CONVERSIONS IN ATLAS

The ATLAS Collaboration

Abstract

The reconstruction of photon conversions in the ATLAS detector is important for improving both the efficiency and the accuracy of the detection of particle decays with photon final states, including $H \rightarrow \gamma\gamma$. In this note the reconstruction of photon conversions for Monte Carlo data is described using both standard inside-out tracking and the more recently implemented outside-in tracking.

1 Introduction

Reconstruction of photon conversions in the ATLAS detector is important for a variety of physics measurements involving electromagnetic decay products. In particular, the efficiency of detection of particles with large-mass diphoton final states, such as the Higgs Boson or the heavy Graviton, is greatly enhanced by proper conversion reconstruction. Conversion reconstruction may also be used for detector-related studies; mapping the locations of the conversion vertices allows one to produce a precise localization of the material in the ATLAS tracker.

As photons may convert at any point in the tracker in the presence of material, the ability to reconstruct conversions will depend strongly on the type of tracking algorithm used. Due to the structure of the ATLAS tracker, photons which convert within 300 mm of the beam axis may be reconstructed with a high efficiency with standard (inside-out) Si-seeded tracking, while photons which convert further from the beam pipe may only be reconstructed using (outside-in) tracks which begin with TRT seeds, with or without associated Si hits. Track reconstruction will be discussed in Section 2, while the reconstruction of conversion vertices will be discussed in Section 3, and the overall reconstruction of conversions will be discussed in Section 4. Applications of photon conversion reconstruction in the case of neutral pion decays and low p_T photons as well as the application of conversion reconstruction to the case of high p_T physics measurements (such as $H \rightarrow \gamma\gamma$), will be found in Section 5. A summary and concluding remarks are found in Section 6.

1.1 Theory

The ATLAS detector is designed to measure, among other things, the energies and momenta of photons produced in high-energy proton-proton collisions. The photons which are relevant to physics measurements will have energies in excess of 1 GeV. These photons must pass through the ATLAS tracker before depositing their energy in the Liquid Argon Calorimeter. At photon energies above 1 GeV, the interaction of the photons with the tracker will be completely dominated by e^+e^- pair production in the presence of material, otherwise known as photon conversion. All other interactions between the photons and the tracker material, such as Compton or Rayleigh scattering, will have cross-sections which are orders of magnitude below that for the photon conversion, and may thus be safely ignored. The leading-order Feynman diagrams for photon conversions in the presence of material are shown in Figure 1. The presence of the material is required in order for the conversion to satisfy both energy and momentum conservation.

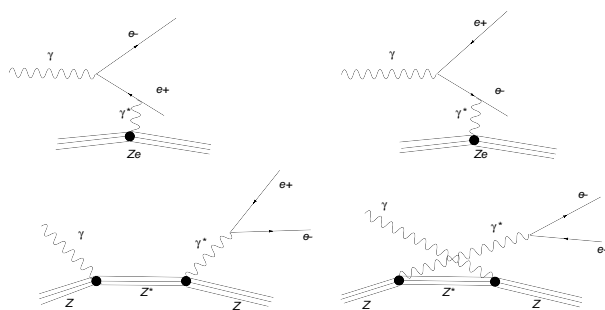


Figure 1: Leading-order Feynman diagrams for photon conversions.

The cross section for the conversion of photons in the presence of material is both well understood theoretically and thoroughly measured. Work on calculating this cross section began almost immediately after the discovery of the positron by Anderson in 1932 [1]. Bethe and Heitler first gave a relativistic

treatment of photon conversion in 1934 [2] in which the screening of the nuclear Coulomb field was taken into account. A detailed review of the theory regarding photon conversion and the calculation of the conversion cross-section for a variety of materials was given by Tsai in 1974 [3]. A more modern treatment of the topic of conversions, including corrections to the Bethe-Heitler formula for photon energies above 5 TeV was given by Klein in 2006 [4].

For photon energies used in this study (1 GeV and above) the cross section for the conversion process is almost completely independent of the energy of the incident photon, and may be given by the following equation [3]:

$$\sigma = \frac{7A}{9X_0N_A}. \quad (1)$$

In this expression A is the atomic mass of the target given in g/mol, and $N_A = 6.022 \times 10^{23}$ is Avogadro's number. X_0 is known as the radiation length of the material through which the photon passes, which for elements heavier than helium may be approximated from the atomic mass A and the atomic number Z by the following relation [5]:

$$X_0 = \frac{716.4 \text{ g cm}^{-2} A}{Z(Z+1)\ln(287\sqrt{Z})}. \quad (2)$$

This radiation length is defined such that it is 7/9 of the mean free path for photon conversion. Plots showing the total radiation length traversed by photons in the tracker before reaching the calorimeter may be found in the next section.

The differential cross section for photon conversions of energies of 1 GeV and above in terms of the quantity $x = (E_{\text{electron}}/E_{\text{photon}})$ is [4]:

$$\frac{d\sigma}{dx} = \frac{A}{X_0N_A} \left(1 - \frac{4}{3}x(1-x)\right). \quad (3)$$

This cross section is symmetric in x and $1-x$, the electron and positron energies, and it implies that the momentum of the photon is not simply shared equally between the electron and the positron. Some fraction of the photon conversions will be highly asymmetric, and either the electron or the positron may be produced with a very low energy. If this energy falls below the threshold required to produce a reconstructable track in the ATLAS tracker, then the converted photon will be seen to have only one track, and will be difficult to distinguish from a single electron or positron. This problem is more serious at lower photon energies, as the proportion of conversions which are asymmetric enough to cause the loss of one of the two tracks increases as the photon energy decreases. The difficulties involved in identifying these highly asymmetric single-track conversions will be discussed in a later section.

1.2 Experimental setup

The ATLAS experiment is a 7000 tonne multi-purpose detector located at the Large Hadron Collider (LHC) at CERN. ATLAS is designed to detect the energies and momenta of highly energetic particles originating from 14 TeV proton-proton collisions at the LHC, at a design luminosity of $10^{34} \text{ cm}^{-2}\text{s}^{-1}$. In this sub-section a very brief description of the ATLAS tracker and electromagnetic calorimeter is included. These are the two sub-systems necessary for the studies relevant to this note. A detailed description of the ATLAS detector can be found in the ATLAS detector paper [6] and references therein.

The coordinate system used for describing the ATLAS detector is briefly summarised here; further details can be found in reference [6]. The ATLAS x , y , and z axes are defined such that the positive x -axis points from the interaction point to the center of the LHC ring, the y -axis is vertical with positive y pointing upwards, and the z -axis lies along the beam direction with side-A of the detector defined

as the positive z direction. The azimuthal angle ϕ is measured around the z -axis, and the polar angle θ is measured from the z -axis. The pseudo-rapidity η is defined as $\eta \equiv -\ln \tan(\theta/2)$. The transverse momentum p_T , and the transverse energy E_T are defined in the $x-y$ plane. Where cylindrical coordinates are used to describe components of the detector, z and ϕ are as above and R is defined as $R \equiv \sqrt{x^2 + y^2}$.

The ATLAS detector consists of several co-axial layers. Starting from the inside of the detector and working outwards the first of these layers is the tracker,

The ATLAS tracker consists of several co-axial layers immersed in a 2T solenoidal magnetic field. In the so-called barrel region, the innermost of these is a pixel detector consisting of three highly segmented cylindrical layers surrounded by four stereo-pair silicon microstrip (SCT) layers. In addition to the cylindrical layers forming the barrel, both the pixel and the SCT also have end-caps consisting of disk shaped segments used for tracking particles with large pseudorapidities ($|\eta| > 1.5$). The outermost portion of the tracker consists of the Transition Radiation Tracker (TRT), which is comprised of many layers of gaseous straw tube elements interleaved with transition radiation material. The TRT is divided into a barrel section, covering the small pseudorapidity region $|\eta| < 1$, and an endcap section covering the large pseudorapidity region $1 < |\eta| < 2.1$. The lack of TRT detector elements at higher pseudorapidities is the reason for all the results presented in this note having a cut off at $|\eta| = 2.1$.

The amount of material in the tracker given in radiation lengths as a function of pseudorapidity can be seen in Figure 2 [6]. As mentioned earlier, the probability of a photon converting in any given layer is proportional to the amount of material in that layer. Overall, as many as 60 % of the photons will convert into an electron-positron pair before reaching the face of the calorimeter [6]. This number varies greatly with pseudorapidity as can be seen in Figure 3 [6], for the case of photons with $p_T > 1$ GeV in minimum bias events. The probability is lowest in the most central region $|\eta| < 0.5$, where the amount of tracker material is greatly reduced. A plot showing the locations of photon conversions in the ATLAS tracker as found in the Monte Carlo from a sample of 500,000 simulated minimum-bias events can be seen in Figure 4 [6]; the three pixel layers and disks as well as the four barrel SCT layers and their corresponding end-cap layers can be clearly seen.

Finally, the energies of the electrons resulting from photon conversions are measured in the electromagnetic calorimeter segments. These are lead-liquid argon detectors with accordion-shaped absorbers and electrodes. Their fine-grained lateral and longitudinal structure, ensures high reconstructed energy resolution for photons with $E_T > 2 - 3$ GeV, as described in reference [7]. Although the daughter electron tracks and the vertices resulting from the converted photons are reconstructed without any calorimetric information, the latter plays a crucial role later in the reconstruction and particle identification process.

2 Track Reconstruction

The current track reconstruction process consists of two main sequences, the primary *inside-out* track reconstruction for charged particle tracks originating from the interaction region and a consecutive *outside-in* track reconstruction for tracks originating later inside the tracker. Both methods reconstruct tracks that have both silicon (Si) and transition radiation tracker (TRT) hits and place these tracks in two distinct track collections. A third track category contains those tracks that have only TRT hits and no Si hits; these TRT-only tracks are placed in their own distinct track collection. All three track collections are then examined to remove ambiguities and double counting and are finally merged into a global track collection to be used later during the vertex-reconstruction phase. For a track to be reconstructed by any of these methods, a minimum transverse momentum $p_T > 0.5$ GeV is required throughout. In the following section, brief descriptions of the various tracking algorithms are provided. More detailed descriptions, in particular of the *inside-out* tracking, can be found in reference [8].

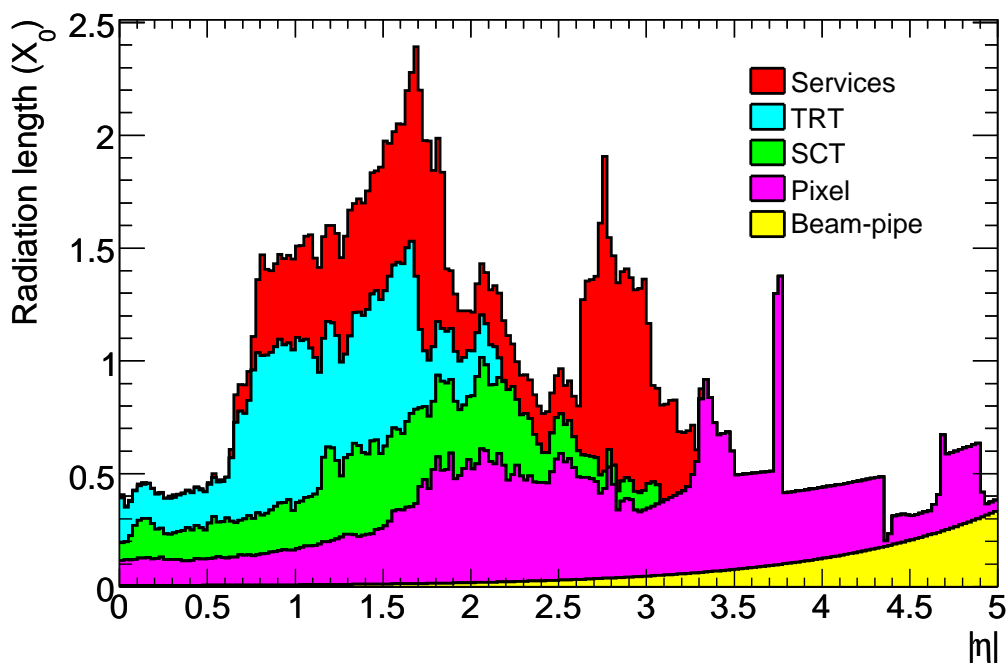


Figure 2: Material in the Inner Detector as a function of pseudorapidity.

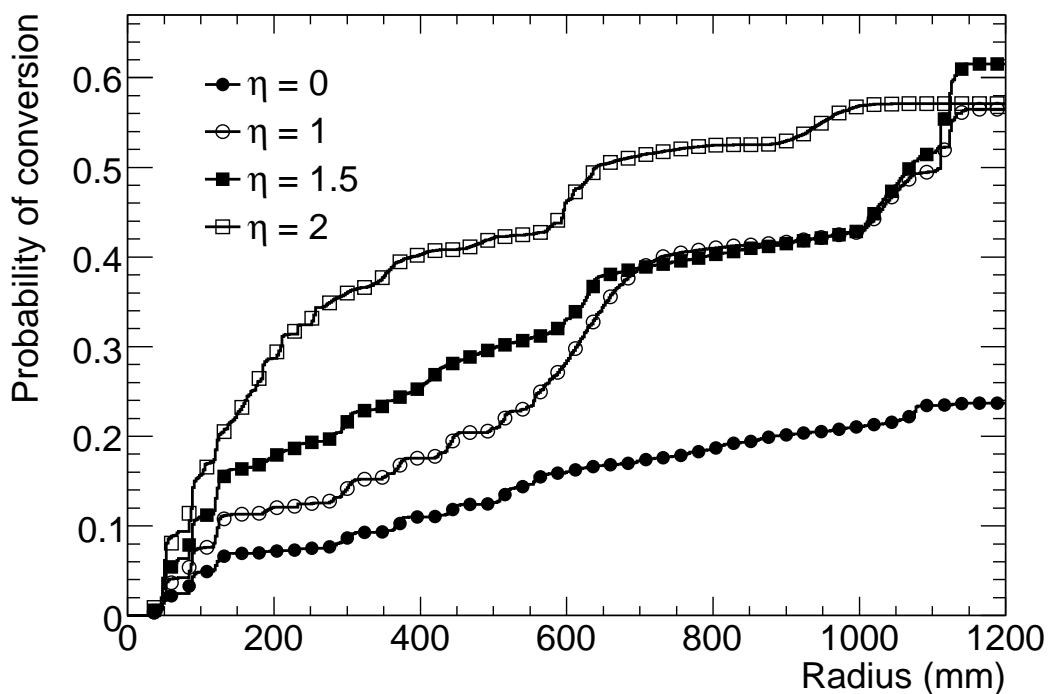


Figure 3: Probability of a photon to have converted as a function of radius for different values of pseudorapidity.

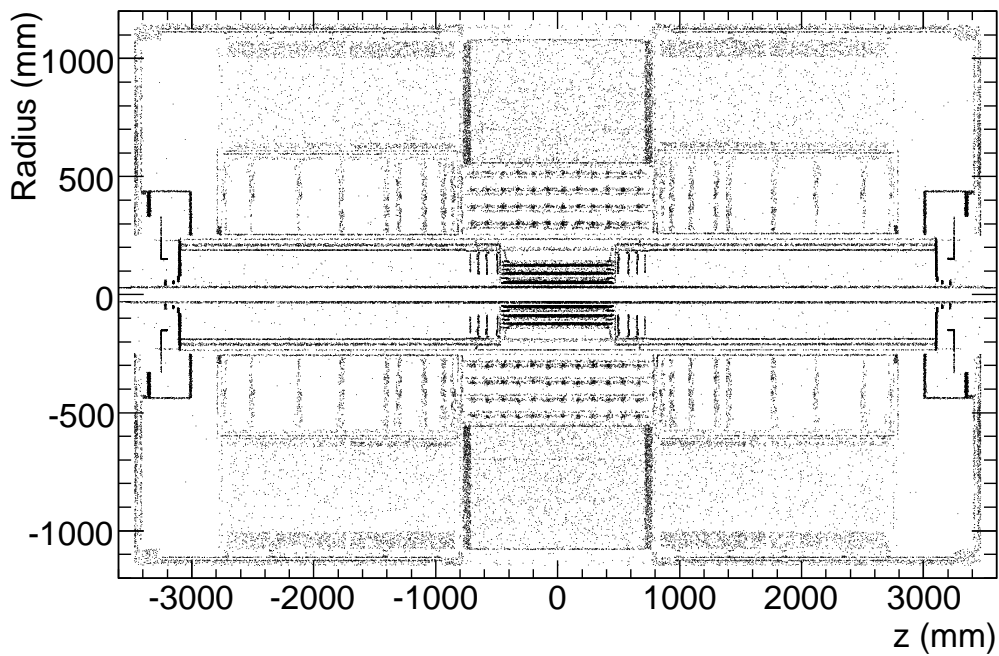


Figure 4: Mapping of the ATLAS tracker using photon conversions (monte-carlo).

2.1 Inside-Out Track Reconstruction

After the reconstruction of space points inside the pixel and SCT sub-detectors, candidate tracks (seeds) are then formed using three space-point combinations. These seeds are subject to some constraints, such as the curvature, to limit the number of possible combinations. Seeds which pass these constraints then become the starting points for reconstructing tracks. Once a seed has been formed a geometric tool is then invoked in order to provide a list of Si-detector elements that should be searched for additional hits. A combinatorial Kalman-fitter/smoothing formalism is then used to add successive hits to the track. The track information is updated after every step in the search and extraneous outlier hits are efficiently eliminated through their large contribution to the χ^2 of the track fit. Not all space-point seeds coming from Si hits result in a track; the rate at which seeds give rise to a fully reconstructed track is on the order of 10% in a typical $t\bar{t}$ physics event.

A large fraction of the reconstructed track candidates either share hits, are incomplete, or may be fakes resulting from random combinations of hits. It is therefore necessary to evaluate the tracks based on a number of quality criteria and score them accordingly, with the score providing an indication of the likelihood of a specific track to describe a real particle trajectory. Tracks with the highest score are refitted and used as the quality reference for all the remaining tracks. Shared hits are removed in this stage and the remaining part of the track is evaluated again and refitted. Track candidates with too many shared hits are then discarded as well as any other track candidate that fails to comply with any of the quality criteria during evaluation.

At this stage, each one of the resolved track candidates is assigned a TRT extension. First, a geometric extension of the Si track is built inside the TRT and compatible measurements are selected. Possible TRT-track extensions are constructed by combining all such TRT measurements. The full track, including any TRT extension, is then refitted and scored in a way analogous to that during the previous ambiguity-resolving stage. If the new track has a quality score which is higher than that of the original Si track,

the TRT extension is kept and added to the Si track, thus creating a “global” Inner Detector track. In other cases only the original Si track is kept, without the TRT extension. The final reconstructed tracks, with or without TRT extensions, are then stored in a dedicated track collection. At this stage they can be classified into three categories:

1. Tracks without TRT extensions (e.g. $|\eta| > 2$);
2. Tracks with extensions which are used in the final fit;
3. Tracks with extensions which are not used in the final fit (outliers).

This last category is characteristic of tracks that have suffered large material interactions as they propagated through the tracker material.

The *inside-out* track reconstruction (as described in the previous section) is a very powerful technique for reconstructing tracks, especially in busy environments where the high granularity of the Si sub-detectors (and in particular that of the pixel detector) can provide the necessary resolution for recovering the track-hit pattern. However, it may also lead to fake tracks if not carefully implemented. In order to reduce the number of fake reconstructed tracks, a minimum number of Si hits is required for a track to be reconstructed; in the present implementation of the algorithm this number is seven. This requirement immediately leads to a decreased efficiency in reconstructing tracks that originate late inside the tracker, i.e. in the SCT. Furthermore, tracks which are present only inside the TRT will not be reconstructed at all. These tracks can appear in the cases of secondary decays inside the tracker (e.g. K_s decays) or during photon conversions, the latter being of special interest to this note.

2.2 Outside-In Track Reconstruction

The *outside-in* track reconstruction (also referred to as back-tracking) can offer a remedy to the inefficiency in reconstructing tracks which originate after the pixel detector.

The starting point for this type of track reconstruction is the TRT, where initial track segments are formed using a histogramming technique. The TRT tracker can be divided in two parts, a barrel and an endcap one, the dividing line being at the $|\eta| = 0.8$ pseudorapidity range. In the $R - \phi$ plane of a TRT barrel region or the $R - z$ plane of a TRT endcap section, tracks that originate roughly at the primary interaction region appear to follow straight lines (this is exactly true in the second case). These straight-line patterns can be characterized by applying the Hough transform [9], which is based on the simple idea that in the $R - \phi(R - z)$ plane, a straight line can be parametrized using two variables: (ϕ_0, c_T) or (ϕ_0, c_z) respectively, where c_T and c_z are the corresponding azimuthal and longitudinal curvatures and ϕ_0 is the initial azimuthal angle. As a result, in a two-dimensional histogram formed by these two parameters, TRT straw hits lying on the same straight line will fall within a single cell. Straight lines can therefore be detected by scanning for local maxima in these histograms. To improve the accuracy in the longitudinal direction, the TRT is divided into 13 pseudorapidity slices on either side of the $\eta=0$ plane. The slice size varies, it being smaller around the TRT barrel-endcap transition region and bigger inside the TRT barrel or endcap regions. The two-variable approximate track parameters can then be used to define a new set of geometric divisions inside the TRT, within which all straws that could possibly be crossed are included. Using the transformation described in [10], the curved trajectory suggested by the straw hits may be transformed into a straight line in a rotated coordinate system. This is the initial step for a “local” pattern recognition process, in which the best TRT segment may be chosen as the one that crosses the largest number of straws in this straight-line representation. A cut on the minimum number of straw hits necessary to consider the segment as valid is applied during this step. A final Kalman-filter smoother procedure is then applied to determine as accurately as possible the final track parameters of the segment. The above TRT-segment reconstruction procedure has been adopted from the original ATLAS track reconstruction algorithm *xKalman* as described in the references [11].

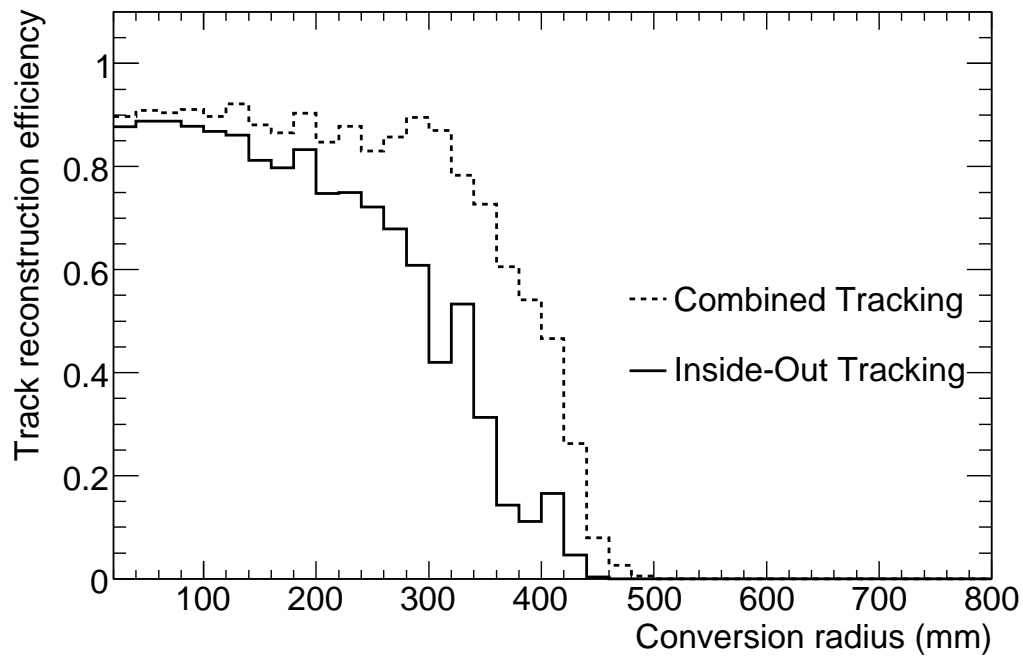


Figure 5: Track reconstruction efficiency for conversions from 20 GeV p_T photons as a function of the conversion radius. The gain in track reconstruction efficiency when tracks reconstructed moving inwards from the TRT are combined with tracks reconstructed by the *inside-out* algorithm, is evident particularly at higher radial distances.

The reconstructed TRT segments are then fed into the second step of the back-tracking algorithm in which extensions are added to them from the Si sub-detectors. Space-point seeds are searched for in narrow $R - \phi$ wedges of the Si tracker, indicated by the transverse TRT-segment track parameters derived in the previous step. A minimum of two space points is required in this case, the search being confined to the last three SCT layers. To reduce the number of space-point combinations cuts on the curvature are then applied, with the third measurement point provided by the first hit in the initial TRT segment. As soon as seeds with pairs of space points are formed, the initial-segment track parameters can then be significantly improved, especially the longitudinal components. A new geometric section through the Si-detector elements is then constructed and a combinatorial Kalman-fitter/smoothen technique, as in the case of the *inside-out* tracking, is applied to produce Si-track extension candidates. The Si-track extensions provide a much improved set of track parameters, which can be used to find new TRT extensions to be assigned to every Si-track candidate, thus creating once more a “global” track. Ambiguity resolving and track refitting follow afterwards in the appropriate manner. The final set of resolved tracks from this process is stored in a dedicated track collection. In order to reduce the time required for the reconstruction and minimize double counting, the *outside-in* tracking procedure excludes all the TRT-straw hits and Si-detector space points that have already been assigned to *inside-out* tracks. The enhancement of the track reconstruction efficiency after the *outside-in* reconstructed tracks are included is shown in Figure 5. Here the track reconstruction efficiency for photon conversions is plotted as a function of the radial distance of the conversion for the case of 20 GeV p_T single photons, before and after the *outside-in* tracking is performed. The bulk of the gain in tracking efficiency is, as expected, at larger radii. The inefficiencies of this method as a function of radius are discussed further in section 2.3 and again in sections 4.3 and 4.4. Due to the more limited pseudorapidity coverage of the TRT tracker, the *outside-in* tracking can be used to efficiently reconstruct tracks up to a pseudorapidity value of $|\eta| = 2.1$. All the results presented here have therefore been restricted to within this pseudorapidity range.

2.3 Standalone TRT tracks. Final Track Collection.

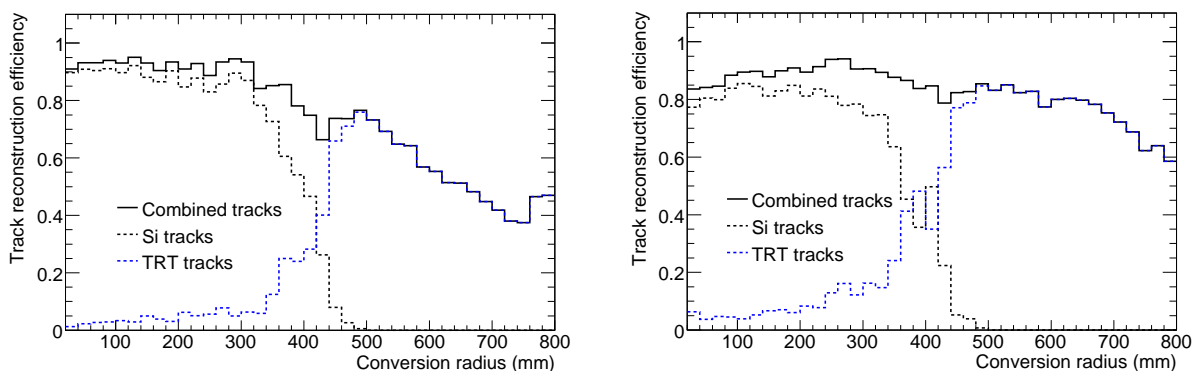


Figure 6: Track reconstruction efficiency for conversions from 20 GeV p_T converted photons (left) and 5 GeV p_T converted photons (right).

After the *inside-out* track collection has been formed, all TRT segments that have not been assigned any Si extensions are then used as the basis of one more distinct track collection. These segments are first transformed into tracks, and the segment local parameters are used as the basis for producing the corresponding track parameters assigned to the surface of the first straw hit. Perigee parameters are also computed, but no overall track refitting is performed. These new TRT tracks are then scored and arranged

accordingly and a final ambiguity resolving is performed in order to reject any tracks that share too many straw hits. Finally, these standalone TRT tracks are then stored in a special track collection.

At the end of the track reconstruction process, and before any primary or secondary vertex fitters are called or other post-processing tasks are executed, the three track collections described above are merged. One last ambiguity resolving is performed in order to select unique tracks from all three collections, although this is mostly for consistency since the straw hits and Si space points associated with the *inside-out* tracks have already been excluded before the *outside-in* track reconstruction. This merged track collection is then used by the photon conversion reconstruction algorithm.

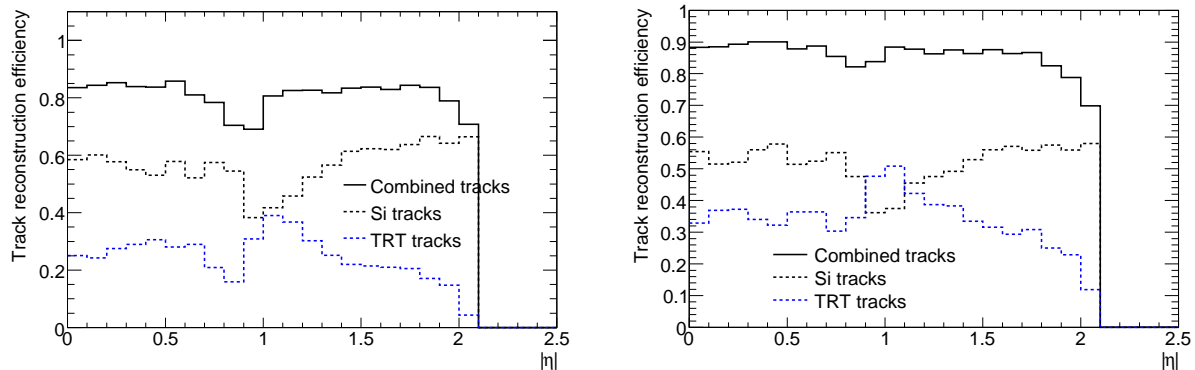


Figure 7: Track reconstruction efficiency for conversions from 20 GeV photons (left) and 5 GeV photons (right) as a function of pseudorapidity.

The overall tracking efficiency after all three track collections discussed above are merged, is shown in Figure 6 for both the case of a 20 GeV p_T single photon sample, and also for a 5 GeV single photon sample, which is more indicative of the case of low track momenta. Two competing effects become apparent as one observes these two plots. The overall track reconstruction efficiency for conversions that happen early inside the tracker, i.e. in $R < 150$ mm, is higher in the case of the 20 GeV p_T photons than that for the 5 GeV p_T ones. This is a clear indication of the larger effect that bremsstrahlung losses have on low p_T tracks, especially on those that originate early inside the tracker. Furthermore it is possible that, depending on the amount of the incurred losses, only part of the track will be reconstructed, i.e. its TRT component, with the pattern recognition failing to recover the corresponding Si clusters. The small fraction of standalone TRT tracks that enhance the track reconstruction efficiency from early conversions, is primarily due to this effect. On the other hand the overall track reconstruction efficiency at higher radii is much better for the case of the 5 GeV p_T photons. This is due to the fact that the radius of curvature, being much larger for those tracks, enables them to separate from each other faster as they traverse the tracker under the influence of the applied magnetic field. It is therefore easier in this case to distinguish the two tracks and reconstruct them during the pattern recognition stage. Figure 7 shows the track reconstruction efficiency as a function of pseudorapidity, for both 20 GeV and 5 GeV p_T photons. The overall track reconstruction efficiency is very uniform along the whole pseudorapidity range, starting only to significantly fall off as one approaches the limit of the TRT pseudorapidity extent ($|\eta| = 2.1$). The reduction in efficiency observed around $|\eta| = 1$, is due to the gap at the transition from the barrel to the end cap TRT. The seemingly higher overall tracking efficiency in this plot compared to that in Figure 6, is due to the fact that the great majority of converted photons originate from the earlier layers of the Si tracker. In this region, as Figure 6 demonstrates, the converted photon track reconstruction efficiency is very high.

3 Vertex Fitting

Track finding is only the first step in reconstructing photon conversions; the next step is being able to reconstruct the conversion vertex using the pair of tracks produced by the converted photon. Reconstruction of the conversion vertex is quite different from finding the primary interaction vertex, since for conversions additional constraints can be applied that directly relate to the fact that the converted photon is a massless particle. A specific vertex algorithm, appropriately modified in order to take into account the massless nature of the conversion vertex, has been developed for use by the photon conversion algorithm.

The vertex fit itself is based on the fast-Kalman filtering method; different robust versions of the fitting functional can also be set up in order to reduce the sensitivity to outlying measurements. The vertex fitting procedure uses the full 3D information from the input tracks including the complete error matrices [12].

3.1 Algorithm Description

The goal of a full 3D vertex fit is to obtain the vertex position and track momenta at the vertex for all tracks participating in the fit as well as the corresponding error matrices. From the input tracks, the helix perigee parameters defining the particle trajectory along with their weight matrix are extracted as described in the references [13, 14]. If one assumes that the particle is created at the vertex \vec{V} , then the trajectory parameters q_i may be expressed as a function of the vertex position and the particle momentum at this vertex $q_i = T(\vec{V}, \vec{p}_i)$. A vertex is then obtained by minimizing:

$$\chi^2 = \sum_{i=1}^2 (q_i - T(\vec{V}, \vec{p}_i))^T w_i (q_i - T(\vec{V}, \vec{p}_i)), \quad (4)$$

where w_i is the 5×5 weight matrix from the track fit. In order to find the \vec{V} and \vec{p}_i which minimize the above χ^2 , equation 4 can be linearized at some convenient point close to the vertex as:

$$\chi^2 = \sum_{i=1}^2 (\delta q_i - D_i \delta \vec{V} - E_i \delta \vec{p}_i)^T W_i (\delta q_i - D_i \delta \vec{V} - E_i \delta \vec{p}_i), \quad (5)$$

where $D_i = (\partial T(\vec{V}, \vec{p}_i)) / (\partial \vec{V})$ and $E_i = (\partial T(\vec{V}, \vec{p}_i)) / (\partial \vec{p}_i)$ are matrices of derivatives. A fast method to find a solution that minimizes equation 5 has been proposed in the references [13, 14]. It can be shown that this method is completely equivalent to a Kalman-filter based approach [15], where the vertex position is recalculated after every new track addition.

If the initial estimation of the vertex position is far from the fitted vertex, then the track perigee parameters and the error matrix are extrapolated to the fitted point, all derivatives are recalculated and the fitting procedure is repeated. The official tracker extrapolation engine, along with a magnetic field description based on the actual measurement of the ATLAS tracker solenoidal field, is used in this case.

3.2 Vertex Fit Constraints

Constraints are included in the vertex fit algorithm via the Langrange multiplier method. A constraint can be viewed as a function

$$A_j(\vec{V}, \vec{p}_1, \vec{p}_2, \dots, \vec{p}_n) = const \quad (6)$$

which is added to the fitting function of equation 4 as

$$\chi^2 = \chi_0^2 + \sum_{j=1}^{N_{const}} \lambda_j \cdot A_j^2 \quad (7)$$

Here χ_0^2 is the function without constraints, λ_j is a Lagrange multiplier and j is the constraint number. $A_j^2(\dots)$ can be linearized around some point $(\vec{V}_0, \vec{p}_{0i})$ to obtain

$$\chi^2 = \chi_0^2 + \sum_{j=1}^{N_{const}} \lambda_j \cdot (A_{j0}^2 + H_j^\top \delta V + \delta V^\top H_j + F_{ij}^\top \delta p_i + \delta p_i^\top F_{ij}) \quad (8)$$

where $H_j = (\partial A_j)/(\partial \vec{V})$, $F_{ij} = (\partial A_j)/(\partial \vec{p}_i)$, A_{j0} is an *exact* value of A_j at the $(\vec{V}_0, \vec{p}_{0i})$ point, $\delta \vec{V} = \vec{V} - \vec{V}_0$ and $\delta \vec{p}_i = \vec{p}_i - \vec{p}_{0i}$.

The solution of equation 8 then has the form $\vec{V} = \vec{V}_0 + \vec{V}_1$, $\vec{p}_i = \vec{p}_{0i} + \vec{p}_{1i}$, where \vec{V}_0, \vec{p}_{0i} is the solution of the corresponding problem without the constraint $\chi^2 = \chi_0^2$. The second component \vec{V}_1, \vec{p}_{1i} of the above solution is obtained through the normal Lagrange multiplier system of equations. In the case of the conversion vertex, a single angular constraint needs to be implemented. This requires that the two tracks produced at the vertex should have an initial difference of zero in their azimuthal and polar angles $\delta\phi_0, \delta\theta_0 = 0$. This is a direct consequence of having an initial massless particle, but it has the advantage of being much easier to implement.

The right-hand plot in Figure 8 shows the reconstructed photon inverse transverse momenta p_T after vertex fitting for conversions where neither of the emitted electrons suffered significant bremsstrahlung ($< 20\%$ of each electron's energy is lost), while the left shows the transverse momenta for the cases where significant bremsstrahlung was present. Similarly the corresponding radial position resolution for conversions with/without significant losses due to bremsstrahlung is shown in Figure 9. Single converted 20 GeV p_T photons were used for the plots above and the emitted electron tracks were required to have at least two silicon space points. The angular constraints $\delta\phi, \delta\theta = 0$, implemented as described earlier, has been used throughout. The overall vertex reconstruction efficiency will be discussed in the following section. It is evident that the presence of bremsstrahlung significantly deteriorates the performance of the vertex fitter.

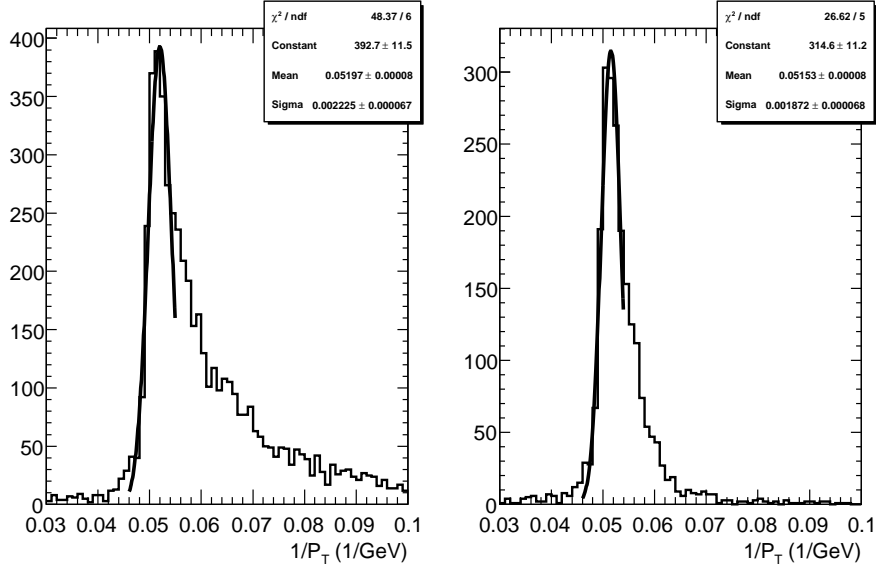


Figure 8: The reconstructed inverse transverse momenta from 20 GeV p_T converted photons with (left) and without (right) significant losses due to bremsstrahlung.

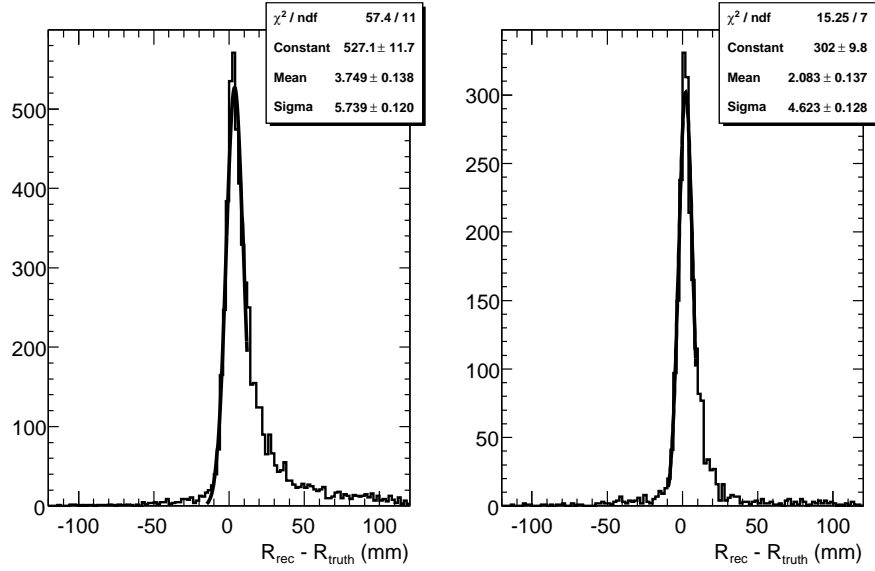


Figure 9: The reconstructed vertex radial positions in mm for conversions from 20 GeV p_T photons as compared to their truth values. The left-hand plot is for conversions with significant bremsstrahlung losses and the right-hand one without.

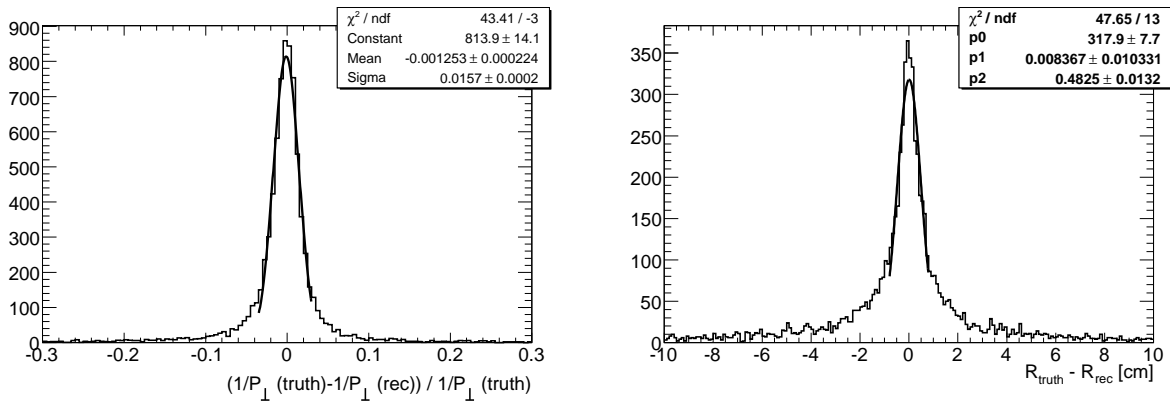


Figure 10: Overall reconstructed $1/p_T$ resolution (left) and radial position resolution (right) for a 10 GeV K_s decay. Only tracks with at least two silicon space points are used.

As a further check of the performance of the vertex algorithm described in this section, one can apply it to the case of the $K_s \rightarrow \pi^+ \pi^-$ decay. The absence of losses due to bremsstrahlung for the pion tracks, as well as the non-zero opening angle, provide a good test scenario for the constrained vertex fitting. Instead of the angular constraint used in the case of the photon conversions, a straightforward mass constraint is implemented in this case. Figure 10 shows the resolution of both the reconstructed $1/p_T$ and the radial position for a 10 GeV K_s decay. The absence of a bremsstrahlung related tail in the left handside plot compared to those in Figure 8 is striking.

In a direct comparison to the photon case, Figure 11 shows the $1/p_T$ resolution with and without significant bremsstrahlung losses (20%) respectively, for a reconstructed 20 GeV p_T converted photon together with that of a 10 GeV p_T K_s , as a function of the distance from the beam axis. In the case of the K_s decays the reconstructed momentum resolution is better than 2% irrespective of the distance from the beam axis, deteriorating only slightly as one moves further away from the beam axis. For the case of the photon conversions though, a deterioration in the transverse momentum reconstruction resolution due to the presence of bremsstrahlung losses, is clearly observable when compared to the K_s case. Due to the bremsstrahlung losses, the reconstructed $1/p_T$ distribution has a non-gaussian shape, characterized by a tail towards the higher $1/p_T$ ranges, as Figure 8 shows. As a result, a gaussian fit when performed on the gaussian core of the $1/p_T$ distribution, will result in a worse overall reconstructed momentum resolution, even in the case of smaller bremsstrahlung losses, as both sides of Figure 11 demonstrate. The effect is even more significant if we recall that the reconstructed converted photons have twice as high initial p_T than the K_s used in the same figure. The fact that the photon is a massless particle, resulting in an extremely small angular opening of the emitted tracks, makes it also more difficult to reconstruct accurately the position of the conversion vertex, as is shown in Figure 12.

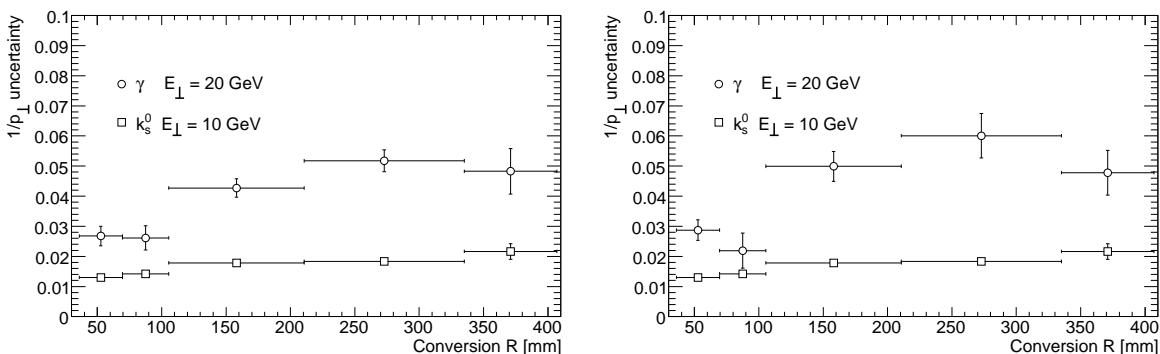


Figure 11: Reconstructed relative $1/p_T$ resolution as a function of distance from the beam axis (mm) for a 20 GeV p_T converted photon and a 10 GeV p_T K_s . In the plot on the left, only converted photons where both their daughter electrons lost $< 20\%$ of their energy due to bremsstrahlung, are shown. In the plot on the right all conversions are included.

4 Conversion Reconstruction

With the three track collections and the vertex fitting algorithm described in the previous two sections, we now have all the necessary tools in place in order to fully reconstruct photons which convert as far as 800 mm away from the primary interaction point. Beyond that radius, the track reconstruction efficiency drops off dramatically due to the lack of a sufficient number of hits in any sub-detector to reliably recon-

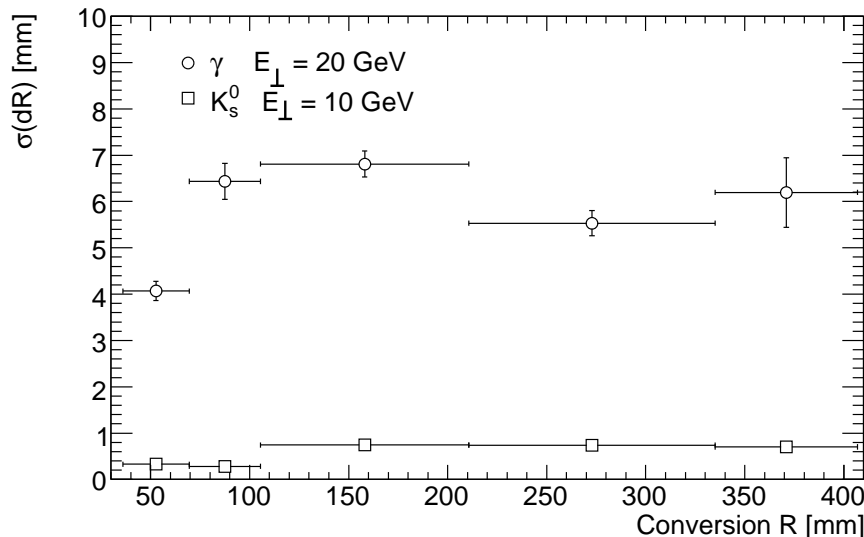


Figure 12: Reconstructed radial resolution as a function of distance from the beam axis (mm) for a 20 GeV p_T converted photon and a 10 GeV p_T K_s . In the case of the photon all daughter electrons regardless of bremsstrahlung losses have been included.

Cut	Efficiency	Rejection
No Cuts	0.7378	1.00
Impact d0	0.7334	1.16
Impact z0	0.7316	1.18
TR ratio	0.7119	2.12

Table 1: Track selection cuts. Cumulative efficiency and rejection rates are presented.

struct the particle trajectory and accurately predict its track parameters. The conversion reconstruction algorithm is run within the framework of the overall Inner Detector reconstruction software; it is one of the last algorithms run during the post-processing phase. The basic components of the conversion reconstruction are: the track selection and subsequent track classification, the formation of pairs of tracks with opposite charge, the vertex fitting and reconstruction of photon conversion vertex candidates, and finally the reconstruction of single track conversions. The conversion candidates are then stored in a separate vertex collection, to be retrieved and further classified through matching with electromagnetic clusters during the next level of the event reconstruction. In the results presented in this section, the reconstruction efficiency is estimated for those photon conversions that happen as far as 800 mm away from the primary interaction point, emit daughter electrons with each having at least $p_T=0.5$ GeV and are within the $|\eta| = 2.1$ pseudorapidity range. This amounts to $\sim 77\%$ of the total photons converted inside the ATLAS tracker volume in the case of the $H \rightarrow \gamma\gamma$ sample.

4.1 Track Selection

Only a fraction of the possible track pairs reconstructed by the tracking algorithms and included in the final track collection come from converted photons. Although the wrong-track combinations may be rejected later during the conversion reconstruction process or by physics specific analysis, it is important

Cut	Efficiency	Rejection
Polar Angle	0.7070	10.8
First Hit dR	0.7049	12.5
Min Distance	0.6994	16.3
dXY	0.6970	16.5
Vertex R	0.6959	16.6
Min Arc L	0.6935	40.3
Max Arc L	0.6890	111.6
dz	0.6870	111.9

Table 2: List of cuts employed during the track pair selection for the three possible types of track pairs. The cumulative efficiency and rejection rate are presented. See text for the definition of the cut variables.

to remove them as efficiently as possible at an early stage, not least because of the large amount of CPU time involved in processing every possible track pair. Cuts on the perigee impact and longitudinal track parameters, as well as the transverse momentum, are first applied. Tracks that are most probably associated to electrons are then selected by cutting on the probability reconstructed by using the ratio of high threshold TRT hits over the total number of TRT hits in each track [16]. These cuts have been tuned using $H \rightarrow \gamma\gamma$ events, with background present due to the undelying event. All the efficiencies and rejection factors due to track selection cuts which are quoted in this note refer to this physics sample. Table 1 shows the performance of these cuts in accepting tracks produced by converted photons and rejecting non-conversion related tracks. The starting efficiency of $\sim 74\%$ reflects entirely the inefficiency of reconstructing all the conversion related tracks during tracking. After applying these cuts, the surviving tracks are then arranged into two groups with opposite charges.

4.2 Track Pair Selection

At this point in the reconstruction process, all possible pairs of tracks with opposite signs are formed and further examined. There are three possible types of track pairs:

1. Pairs in which both tracks have Si hits;
2. Pairs in which one of the two tracks is a standalone TRT track;
3. Pairs in which both tracks are standalone TRT tracks.

In order to reduce the combinatorial background, a series of cuts are applied during the pair formation. These are common to all three track pair types described above, although their actual values may differ. Table 2 lists those cuts along with the corresponding efficiencies and rejection factors for selecting the correct track pairs and discarding fakes resulting from wrong track combinations. The first criterion for accepting a track pair is that the difference in polar angles between the two daughter tracks in a conversion should be small, based on the fact that the photon is massless. Furthermore, the distance between the first hits of the two tracks in the pair should be reasonably close; this is particularly true in the case where both of them are standalone TRT tracks. Finally, the distance of minimum approach between the two tracks in the pair is checked. An iterative method has been implemented that uses the Newton approach to find the set of two points (one on each track) which are closest to each other. The distance of minimum approach between the two tracks is then calculated and a cut is applied to reject those cases where the tracks fail to come within a specified distance from each other.

In order to enhance the performance of the constrained vertex fitter, it is important to begin with a reasonable initial estimate of the vertex position. Using the perigee parameters of the two tracks in

the pair, the corresponding radius of curvature and the center of curvature of the track-helix projection on the $R - \phi$ plane can be derived. As this track-helix projection is circular in the case of a uniform magnetic field such as that of the ATLAS tracker, the estimated vertex position can be identified as either the point of intersection of two circles, or in the case of non intersecting circles, as the point of minimum approach between two circles. If the two circles do not intersect or approach each other closer than a set minimum distance then the pair is discarded. In principle, two circles may intersect at two points. Since two tracks originating from a conversion vertex (or any vertex for that matter) should also intersect on the $R - z$ plane, the correct intersection point on the $R - \phi$ plane is then chosen to be the one which is closer to the point of minimum approach of the two tracks on the $R - z$ plane. The points of minimum approach both on the $R - \phi$ and the $R - z$ planes should clearly be sufficiently close to each other. If they are separated by more than a set minimum distance, then the track pair is discarded. A cut is also applied on the arc length of the $R - \phi$ plane projection of the two track helices between the line connecting the centers of curvature of the two circles and the actual intersection points. This arc length is required to fall within a specific range which again ideally should tend to be very small. Finally, the distance from the track origin (the candidate conversion vertex location) and the actual points of intersection should also be small. Only track pairs with intersection or minimum approach points that satisfy the above criteria are further examined. Estimating the initial vertex position allows for a larger number of quality criteria of the track pair to be used in the overall selection process. All the cuts applied during this step have been tested using the 120 GeV $H \rightarrow \gamma\gamma$ physics sample; the cuts are tuned so that at least two orders of magnitude of the combinatorial background can be rejected at this point without significant loss in overall conversion reconstruction efficiency. As a consequence cut values have been intentionally kept fairly loose since even correct track pairs could be characterized by less than optimal selection quantities. This is especially true in cases where at least one of the two tracks involved has only TRT hits resulting in reduced reconstructed track parameter accuracy along the z-axis, or in cases where the tracks have suffered substantial bremsstrahlung losses during their propagation through the ATLAS tracker. In general, the position of the initially estimated vertex falls within a few millimeters of the actual conversion vertex for the correct pair combinations, all deviations being due to the reasons mentioned just before.

4.3 Vertex fitting

The original track perigee assigned during the track reconstruction process is set at the primary interaction point and for the case of photon conversions, especially those that happen far inside the tracker, this is a rather poor assignment. Using the initial estimate for the vertex position described previously, we can redefine the perigee at this point. The new perigee parameters need to be recomputed by carefully extrapolating from the first hit of each track in the pair to this new perigee, taking into account all the material encountered on the way. It is these tracks with their newly computed perigee parameters that are passed to the vertex fitter. This also has the desirable effect of avoiding long extrapolations during the various iterations of the vertex fitting process, which might lead to distortions due to unaccounted-for material effects. At the end of the process the new vertex position along with an error matrix and a χ^2 value for the fit are computed. A vertex candidate is then reconstructed that also contains the track parameters as they are redefined at the fitted conversion vertex. The fit is always successful in the case of the correct track pairs, and it often fails otherwise. After the fit is executed, post-selection cuts on the χ^2 of the fit, on the reconstructed photon invariant mass and on the reconstructed photon p_T can be applied, to reduce even further the wrong pair combinations. These are listed in Table 3.

The track pair selection and the vertex fitting process result in a reduction in the combinatorial background rate by more than 2 orders of magnitude, with only a rather small ($\sim 8\%$) loss in overall conversion reconstruction efficiency, in the case of the 120 GeV $H \rightarrow \gamma\gamma$ physics sample. A more quantitative description of the conversion reconstruction efficiency in the Higgs sample will be presented in section

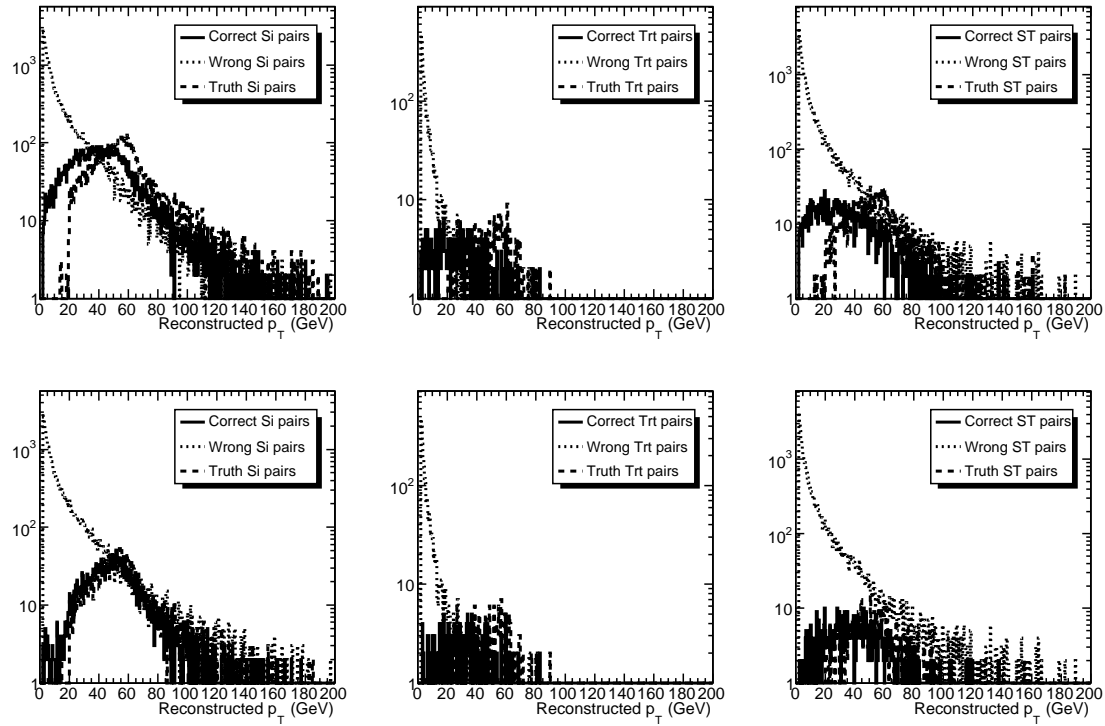


Figure 13: Transverse momentum distribution of reconstructed photon conversions for both correct and wrong track pairs for all three types of pairs: Si-Si (left column), Si-TRT (center column), and TRT-TRT (right column). In the top row all electron tracks regardless of bremsstrahlung energy losses are considered for the case of the correct track pairs. In the bottom row only track pairs where both electrons have lost less than 20% of their energy due to bremsstrahlung are shown. For comparison the truth p_T of the converted photon is also shown.

Cut	Efficiency	Rejection
Fit Convergence	0.6870	171.5
Fit χ^2	0.6710	288.9
Invariant Mass	0.6626	353.9
Photon p_T	0.6625	377.1

Table 3: Post-vertex fit selection cuts. Cumulative efficiency and rejection rates are presented.

5.3. At this stage of the conversion vertex reconstruction, which is still within the Inner Detector software framework, vertices which come from the combinatorial background outnumber the correct conversion vertices by almost a factor of six. The main part of this remaining background consists of reconstructed vertices where at least one of the participating tracks is not an electron at all. This is primarily due to the rather weak particle identification capabilities of the tracker without any access to the electromagnetic calorimeter information. Part of this background can be reduced by some more stringent requirements on the reconstructed conversion vertices after the constrained fit is preformed. But effective improvement is only expected during the subsequent stages of the photon conversion reconstruction, when information from the calorimeter becomes available. Use of the electromagnetic calorimeter should also help to reduce a different type of combinatorial background originating when two electrons from different sources are combined in order to form a track pair. Recent studies indicate significant reduction of both types of the combinatorial background, both by applying tighter vertex selection criteria after the vertex fit is performed and by using the electromagnetic calorimeter information, although they are beyond the scope of this note. The possibility of using the reconstructed photon p_T in order to reduce the number of reconstructed fake vertices, is worth investigating. Figure 13 shows the p_T distribution of the reconstructed conversion vertices along with the distribution for fake vertices resulting from wrong combinations. It is clear that the latter tend to concentrate at the lower p_T region. Nevertheless a final cut on the reconstructed photon p_T will not be as efficient as expected, due to the limited ability at present to correct the reconstructed track momentum for losses due to bremsstrahlung. This is evident in the figure when comparing the reconstructed converted photon p_T distribution with (top row) and without (bottom row) significant bremsstrahlung losses. It becomes even more striking once it is compared to the truth p_T distribution of the converted photon. In the remaining part of this section, the overall performance of the conversion reconstruction software, without utilising the electromagnetic calorimeter information, is examined in the case of single 20 GeV p_T photons, where the combinatorial background is minimal.

Figure 14 shows the track, track pair, and vertex reconstruction efficiencies for conversions coming from 20 GeV p_T photons as a function of both conversion radius and pseudorapidity. Both the track and track pair efficiencies shown in the figure are measured before any of the selection criteria described above are applied. The large drop in the efficiency at $R > 400$ mm is primarily due to the inefficiency of reconstructing both tracks in the track pair from the photon conversion. The ATLAS detector paper version of the plot showing reconstruction efficiency as a function of conversion radius can be found in the appendix in Figure 25. It is noteworthy that both the track and the conversion vertex reconstruction efficiency are essentially constant as a function of pseudorapidity. Finally, Figure 15 shows the overall vertex reconstruction efficiency for converted photons with low transverse momenta as a function of conversion radial position. The two competing effects, the bremsstrahlung losses that affect more severely the low p_T tracks, and the higher radii of curvature that result in increased resolving ability of the smaller p_T tracks, that were discussed in section 2.3, are once more evident here.

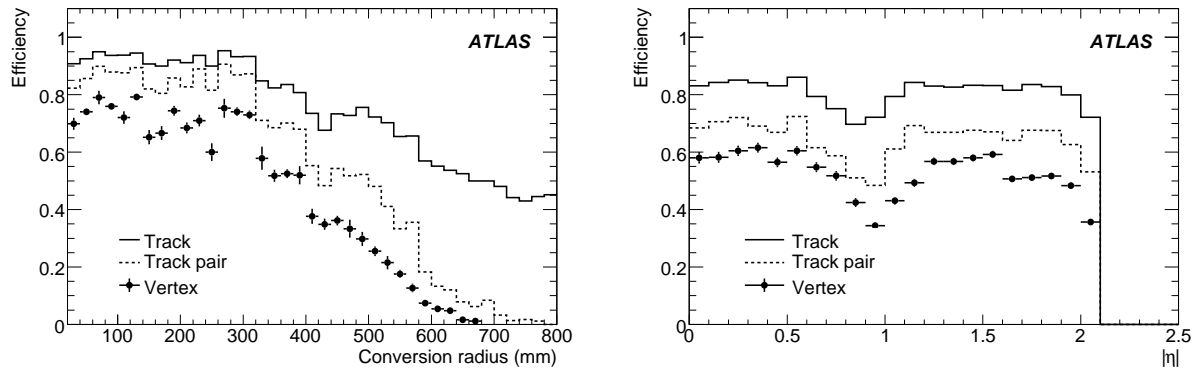


Figure 14: Conversion reconstruction efficiency for conversions from 20 GeV p_T photons as a function of conversion radius (left) and pseudorapidity (right). The solid histogram shows the track reconstruction efficiency, the dashed histogram shows the track-pair reconstruction efficiency, and the points with error bars show the conversion vertex reconstruction efficiency.

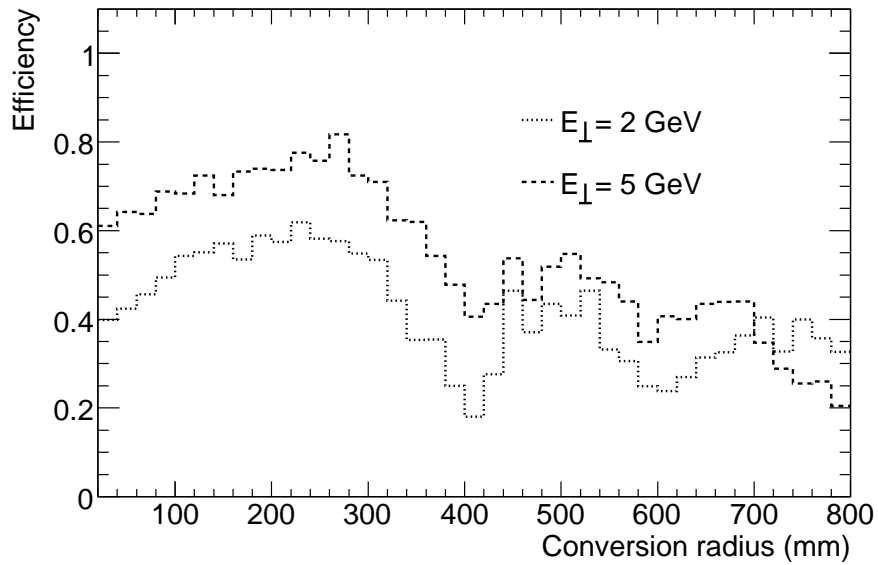


Figure 15: Conversion vertex reconstruction efficiency for photons with 2 and 5 p_T .

4.4 Single Track Conversions

Due to conversions which decay asymmetrically (as described in Section 1.1), as well as cases where the conversion happens so late that the two tracks are essentially merged, there are a significant number of conversions where only one of the two tracks from the photon conversion is reconstructed. Depending on the photon momentum scale, these “single track” conversions become the majority of the cases for conversions that happen late in the tracker and especially inside the TRT. The ability of the TRT to resolve the hits from the two tracks is limited, especially if those tracks do not traverse a long enough distance inside the tracker for them to become fully separated. As a result, only one track is reconstructed, but it may still be highly desirable to recover these photon conversions.

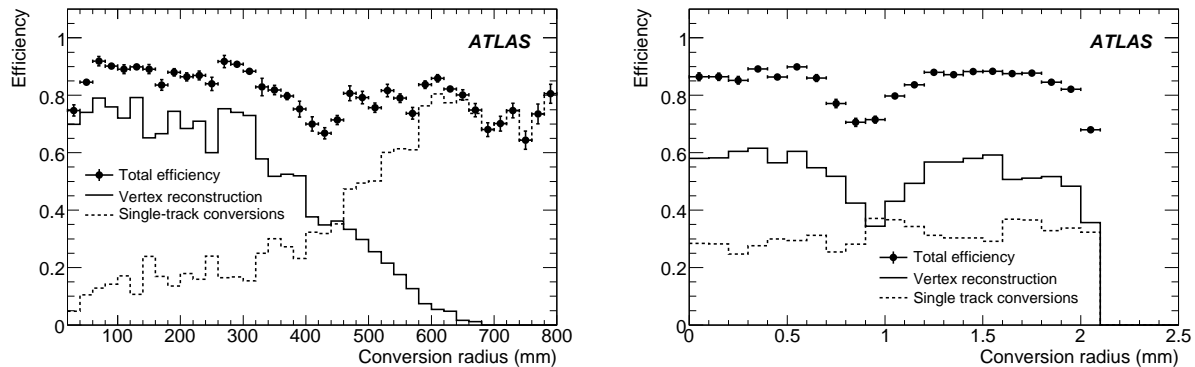


Figure 16: The left hand plot shows the conversion reconstruction efficiency for conversions from 20 GeV p_T photons as a function of conversion radius. The points with error bars show the total reconstruction efficiency, the solid histogram shows the conversion vertex reconstruction efficiency, and the dashed histogram shows the single-track conversion reconstruction efficiency. The right hand plot shows the same efficiencies as a function of pseudorapidity.

At the end of the vertex fitting process, all of the tracks that have been included in a pair that successfully resulted in a new photon conversion vertex candidate, are marked as “assigned” to a vertex. The remaining tracks are then examined once more on an individual basis in order to determine whether or not they can be considered as products of a photon conversion. For a track to be considered, it should have its first hit beyond the pixel vertexing layer. Furthermore, the track should be electron-like, where again the probability reconstructed by using the ratio of the high threshold TRT hits over the total number of TRT hits (as in the initial track selection described earlier in this section, but requiring a much higher value) is used to select likely electron tracks. At the end of this selection tracks wrongly identified as emerging from photon conversions, outnumber the actual photon conversion electron tracks, by almost a factor of two. These are tracks which are not electrons at all, misidentified as such due to the inherent weakness of the particle identification process without the presense of any information from the electromagnetic calorimeter.

A conversion vertex candidate is then reconstructed at the position of the first track hit. It is clear that, especially in the case where the first hit is inside the Si part of the tracker, the position of the conversion vertex reconstructed in this way can be off by as much as a detector layer. This discrepancy is normally much smaller in the case of a vertex inside the TRT due to the higher straw density. On the technical side, this type of reconstruction requires a careful transformation of the local track parameters and error matrix into global ones that are directly assigned to the newly defined vertex. A new vertex candidate is then stored, identical in structure to the one derived from a vertex fit with the important difference

that it has only one track assigned to it. The effect of including the single track conversions into the overall conversion reconstruction efficiency is significant as is shown in Figure 16. The plot shows the conversion reconstruction efficiency for 20 GeV p_T photons as a function of both radial distance and pseudorapidity. As expected, the single-track conversions become more and more dominant at higher radial positions, and single-track conversions are fairly uniformly distributed across the full pseudorapidity range. In comparison, Figure /reffig:singletrackradius2 in the appendix shows the version of the same figure included in the ATLAS detector paper.

5 Physics Applications: Low p_T conversions, γ/π^0 separation, $H \rightarrow \gamma\gamma$

In this section some interesting applications of the usage of the photon conversions are presented. Only results from photon conversions where both of the daughter electron tracks have been reconstructed are included. It needs to be stressed at this point, that everything that is presented here is meant only as an application example and no full scale analysis has been made.

5.1 Low p_T photon conversions

Of particular interest during initial data taking is the use of the reconstruction of converted photons as a tool to obtain a measurement of the amount of material inside the ATLAS tracker, including passive material. The abundance of low p_T neutral pions in minimum bias events represents a very rich source of photons and makes this approach particularly promising. The number of photon conversions measured on a detector volume of known x/X_0 can be used as a normalization point to extract the amount of material at any other location inside the detector by counting the relative number of conversions occurring in that portion. To obtain an unbiased map of the tracker material it is necessary to correct the measured number of conversions by the conversion reconstruction efficiency. Several methods are being investigated to measure this efficiency from data, e.g. embedding Monte Carlo photon conversions in data or extracting it from the measure of decays with similar topology like $K_s^0 \rightarrow \pi^+ \pi^-$.

Figure 17 shows the reconstructed radial positions of photon conversions with 5 GeV p_T . A few structures may be identified: the initial peak caused by the beampipe, the three layers of the pixel detector and then with lower resolution and significance the SCT layers and the TRT. The observed smearing of the reconstructed position of the conversion vertex is mainly due to bremsstrahlung effects. The position resolutions (in the radial direction) of the reconstructed conversion vertex, for photon conversions produced by the decay of neutral pions with various energies, are shown in Figure 18 as a function of the distance from the beam axis. All conversions regardless of the amount of energy lost due to bremsstrahlung by the daughter electrons, have been used. In the case of the lower p_T neutral pions, more relevant in the case of minimum bias events, the radial position resolution improves somewhat, as might be expected from the larger angular separation between the produced electrons. On the other hand the use of low p_T tracks can be limited by the lower tracking efficiency caused by multiple scattering and especially bremsstrahlung.

In order to be able to determine the amount of material at a given position, it is necessary to compare the number of reconstructed converted photons at that position with the number of conversions reconstructed at the position of some reference point. This necessitates being able to resolve the position of the reference, which may not be trivial.

5.2 γ/π^0 Separation

Another application of conversion reconstruction is the possibility of using the converted photons to identify, and subsequently remove, neutral pions in which at least one of the photons resulting from

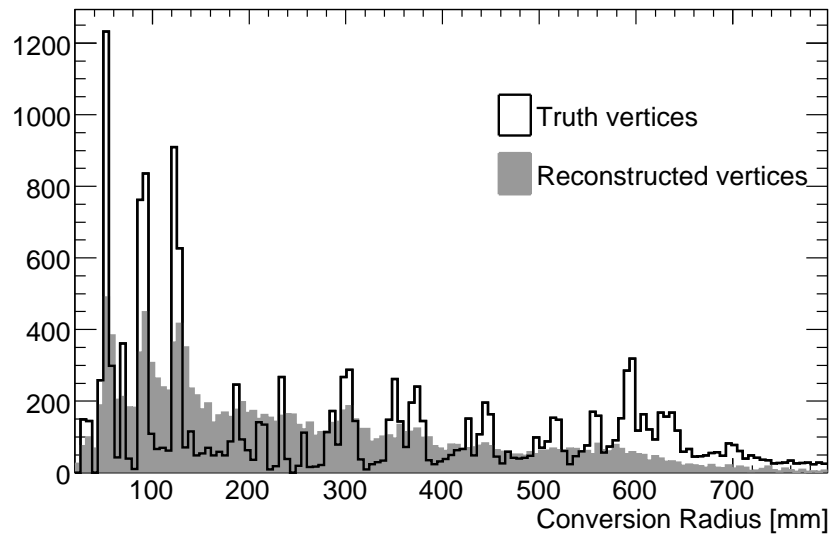


Figure 17: Reconstructed radial positions for conversions of 5 GeV p_T photons. The black histogram shows the truth radial position of the conversion vertices, and the gray histogram shows the radial positions of the reconstructed vertices, regardless of the bremsstrahlung losses of their daughter electrons.

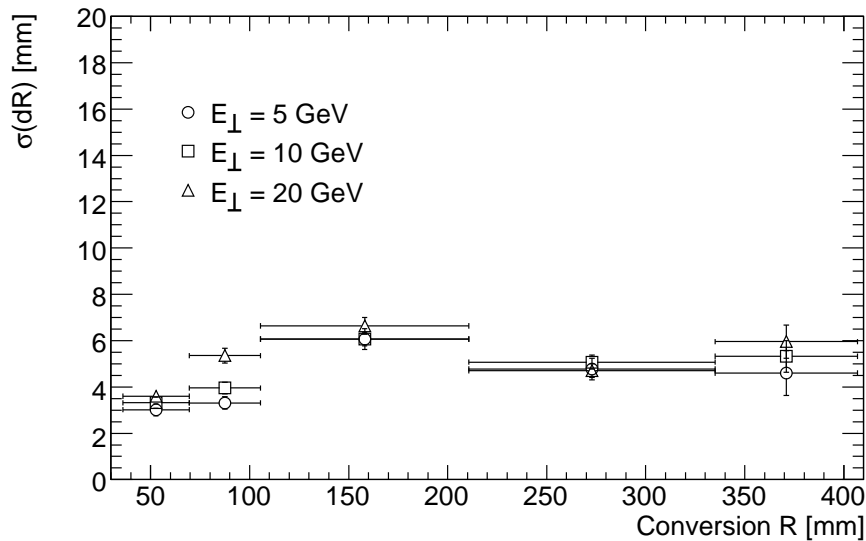


Figure 18: Reconstructed radial position resolution for converted photons produced by the decay of neutral pions with various energies.

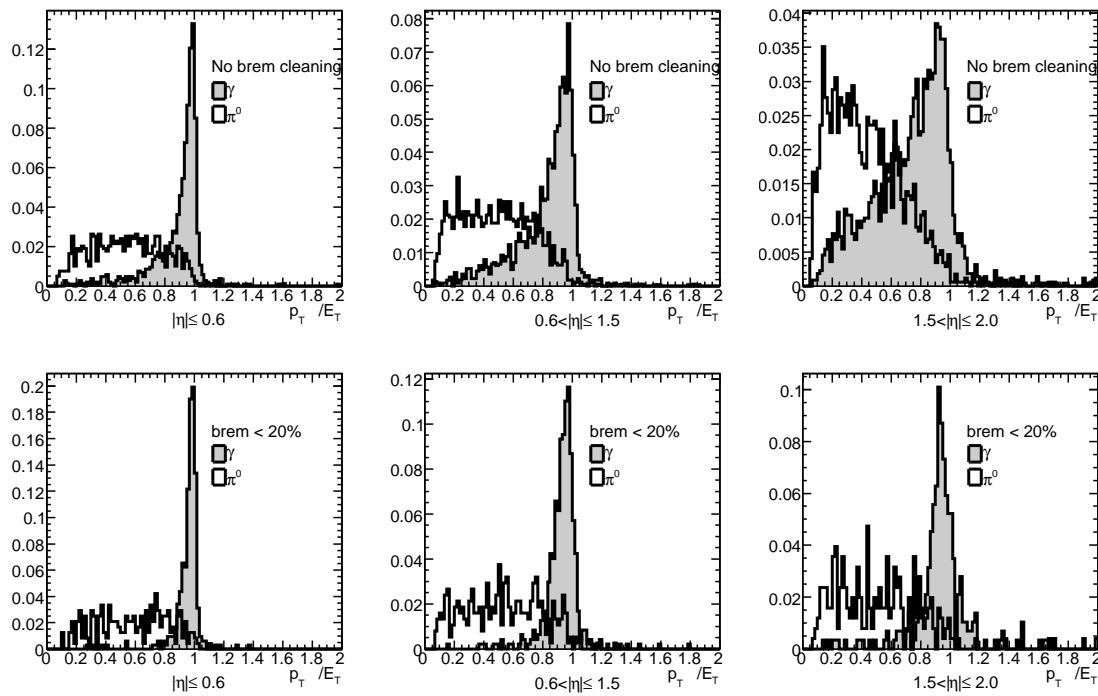


Figure 19: p_T/E_T distribution for 20 GeV p_T converted photons and for photons from a 20 GeV π^0 . The top row shows the distribution for all photons irrespective of the daughter electron energy losses due to bremsstrahlung. The bottom row shows the distribution only for those photon conversions in which the daughter electrons have lost $< 20\%$ of their energies to bremsstrahlung. Three different pseudorapidity ranges are shown, corresponding to the tracker barrel (left), barrel-endcap transition (center) and endcap (right) regions.

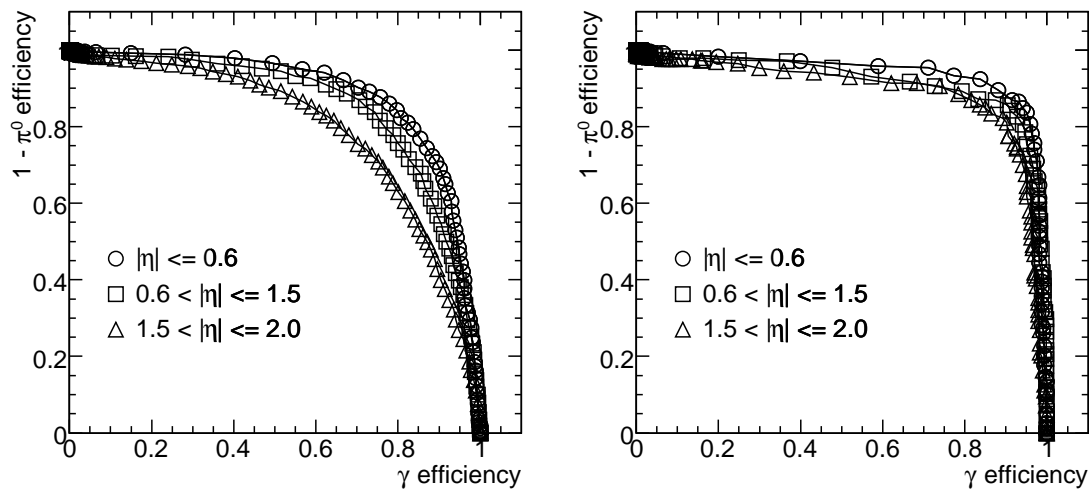


Figure 20: Fraction of remaining π^0 as a function of converted photon efficiency with (left) and without (right) significant bremsstrahlung losses of the corresponding daughter electrons, for three pseudorapidity regions as described in the text.

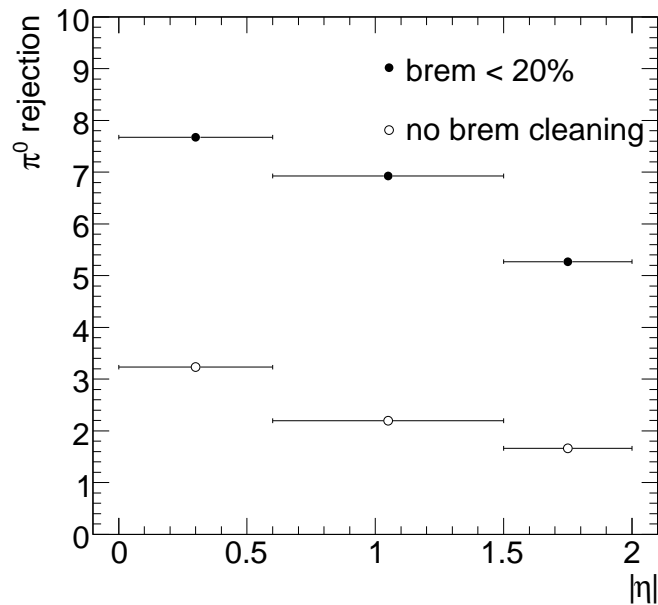


Figure 21: Rejection factors for π^0 corresponding to photon acceptance efficiencies of 90 %, with and without significant energy losses due to bremsstrahlung for the three pseudorapidity regions described in the text. 20 GeV p_T converted photons and π^0 are used.

the decay of the pion has converted. Low multiplicity pions constitute the dominant background to the photon signal after all the calorimeter-specific cuts have been applied during photon identification [17]. In the case of converted photons from π^0 decays, additional handles could be derived as soon as their reconstructed transverse momentum is made available. About 30% of the neutral pions will have at least one of their daughter photons converted and subsequently reconstructed as such, thus providing an estimate of their p_T .

The transverse momentum reconstruction resolution is important when attempting to use conversions to identify low p_T neutral pions. The ratio of the reconstructed p_T of a converted photon inside the ATLAS tracker to the E_T measured by the electromagnetic calorimeter is different for photons from π^0 decays and for prompt photons. Figure 19 shows such distributions for the case of converted 20 GeV p_T single photons and converted photons from the decay of a 20 GeV p_T neutral pion. The photon p_T shown is that reconstructed by the conversion algorithm, while the E_T shown is taken from the truth value from the simulation. Three regions in pseudorapidity are shown separately, namely those corresponding approximately to the tracker barrel, barrel-endcap transition and endcap regions. The top row of plots include all converted photons, irrespective of losses due to bremsstrahlung of their daughter electrons, while the bottom row has only those converted photons where both of their daughter electrons have lost < 20% of their energy due to bremsstrahlung. Clearly the distinction between conversions from single photons and conversions from photons produced in neutral pion decays is less pronounced in the case of strong bremsstrahlung losses, although an effective bremsstrahlung recovery mechanism should be able to significantly improve the separation between the two distributions. A certain degradation is also evident as we move from the barrel to the endcap tracker, due to the less accurate reconstruction of the transverse momentum of the daughter electron tracks at higher pseudorapidities. Figure 20 shows the fraction of remaining π^0 particles as a function of converted photon efficiency, both with and without significant losses due to bremsstrahlung. The overall π^0 rejection corresponding to a photon acceptance

of 90 % for the three different pseudorapidity regions, as described above, is shown in Figure 21. Again a distinction is made for the cases with and without significant energy losses due to bremsstrahlung. Although reduced, the discriminatory power against π^0 is significant even when severe losses due to bremsstrahlung are present.

5.3 $H \rightarrow \gamma\gamma$

As mentioned in the introduction, the recovery of converted photons is of primary importance in the search for physics processes in which photons are the primary decay product. In particular, accurate reconstruction of the $H \rightarrow \gamma\gamma$ process is heavily dependent on the ability to properly reconstruct photon conversions, for the following reasons:

1. A significant fraction of photons will convert inside the ATLAS tracker volume. Efficient reconstruction of these photons, will enhance the signal statistics for this process.
2. Photon identification, using a combination of Inner Detector and Electromagnetic Calorimeter based criteria, will be improved with effective conversion reconstruction. Even single track conversions will be useful in this context.
3. The Electromagnetic Calorimeter calibration will be significantly enhanced when converted photons are identified as such. Again, even single track conversions will be very useful.
4. The ability to accurately point back to the mother Higgs particle is dramatically enhanced for the case of reconstructed converted photons where both daughter electron tracks are properly recovered.

It will be important, therefore, to investigate the performance of the conversion reconstruction strategy in this case, not least because of the higher transverse momenta that characterize the photons produced in $H \rightarrow \gamma\gamma$. A Standard Model Higgs with 120 GeV mass has been assumed throughout this section.

Figure 22 shows the converted photon reconstruction efficiency as a function of both radius and pseudorapidity for photons coming from $H \rightarrow \gamma\gamma$ decay. The reduced efficiency at higher radii is primarily due to the smaller distance which the produced electron tracks travel inside the magnetic field, reducing the separation between them. The conversion reconstruction efficiency as a function of the pseudorapidity is fairly flat, independent of the material distribution inside the ATLAS tracker, as expected. The reconstructed conversion vertex radial position resolution is shown in Figure 23 for reconstructed converted Higgs photon vertices where the participating tracks have lost $> 20\%$ ($< 20\%$) of their energy due to bremsstrahlung, along with all vertices put together. The results are fairly comparable to the ones shown for single photons in section 4, despite the fact that the resulting photon momenta in this case are on average at least a factor of two bigger and the fact that the presence of the underlying event causes additional complications for the track reconstruction.

Of particular interest for the reconstruction of the Higgs invariant mass is the resolution on the measurement of the polar angle of the reconstructed converted photon. This is shown in Figure 24 for the case of conversions where both electron tracks have Si hits. These account for $\sim 58\%$ of the reconstructed converted photons inside the ATLAS tracker volume. The resulting resolution is of the order of 0.5 mrad regardless of the transverse momentum of the converted photon. This is an improvement of at least an order of magnitude with respect to the polar angle resolution derived using the electromagnetic calorimeter response [6].

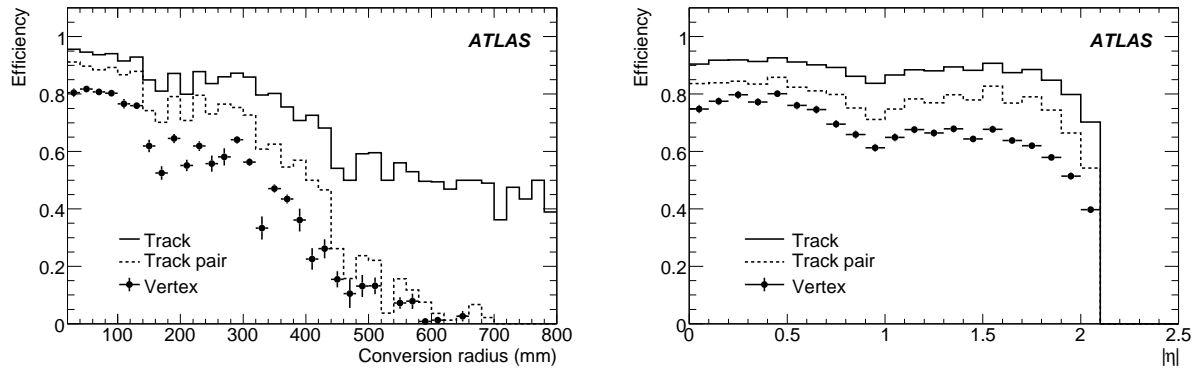


Figure 22: Track, track pair reconstruction, and vertexing efficiency for converted photons from a 120 GeV $H \rightarrow \gamma\gamma$ decay, as a function of distance from the beam axis (left) and pseudorapidity (right). The efficiency reduction at $|\eta| \sim 0.8$, is due to the track reconstruction inefficiencies in the gap region between the TRT barrel and endcap sectors.

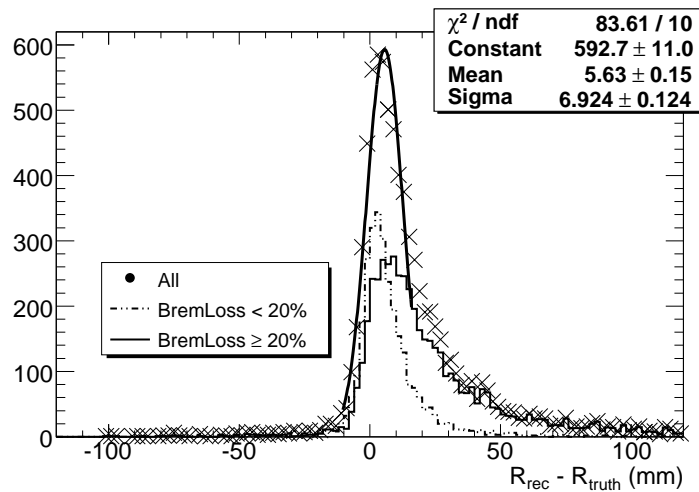


Figure 23: Reconstructed vertex radial position resolution (in mm) for converted photons from a 120 GeV $H \rightarrow \gamma\gamma$ decay. For comparison the two cases where the participating tracks have lost $> 20\%$ ($< 20\%$) of their energy due to bremsstrahlung are also shown separately.

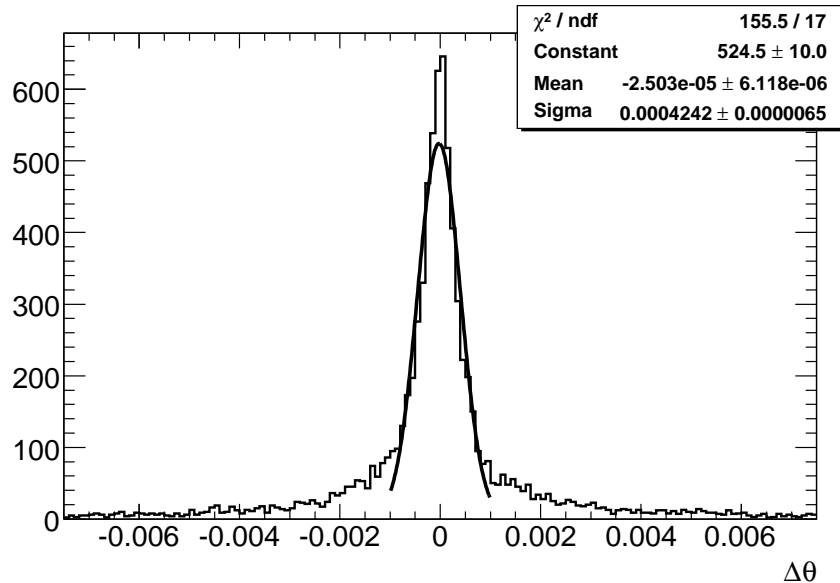


Figure 24: Reconstructed polar angle resolution (in radians) for converted photons from a 120 GeV $H \rightarrow \gamma\gamma$ decay.

6 Summary and conclusions

We have described and presented a detailed performance of the conversion reconstruction algorithm that will be employed by the ATLAS offline software. All three track collections delivered by the tracking software have been combined and used. A dedicated vertex fit algorithm has been developed for the purpose of reconstructing converted photon vertices. Special care has been given to flagging possible conversions where only one of the produced electron tracks has been reconstructed. Combining all of these tools, a reconstruction efficiency of almost 80% has been achieved for conversions that occur up to a distance of 800 mm from the beam axis. A transverse momentum reconstruction resolution has been found to be of the order of 5% for converted single photons of various energies. This has also been shown to be valid for the case of photons produced by the decay of a Standard Model 120 GeV Higgs particle, as well as for those coming from the decay of low p_T neutral pions. The position resolution is found to be better than 5 mm in the radial direction, making this a promising method for mapping the material inside the ATLAS tracker. The angular resolution is found to be below 0.6 mrad, giving effective pointing to converted photons from physics processes.

7 Acknowledgements

We are greatly indebted to all CERN's departments and to the LHC project for their immense efforts not only in building the LHC, but also for their direct contributions to the construction and installation of the ATLAS detector and its infrastructure. We acknowledge equally warmly all our technical colleagues in the collaborating institutions without whom the ATLAS detector could not have been built. Furthermore, we are grateful to all the funding agencies which supported generously the construction and the commissioning of the ATLAS detector and also provided the computing infrastructure.

References

- [1] C.D. Anderson, Phys. Rev. **41** (1932) 405.
- [2] H.A. Bethe, and W. Heitler, Proc. R. Soc. A **146** (1934) 83.
- [3] Y.S. Tsai, Rev. Mod. Phys. **46** (1974) 815.
- [4] S.R. Klein, Radiat. Phys. Chem. **75** (2006) 696.
- [5] Particle Data Group, J. Phys. G: Nucl. Part. Phys. **33** (2006) 263.
- [6] ATLAS Detector Paper - submitted for publication.
- [7] ATLAS CSC note EG6 - Electromagnetic Calorimeter Calibration and Performance.
- [8] T. Cornelissen et al., ATL-SOFT-PUB-2007-007 (2007).
- [9] R. Duda and P. Hart, Comm. ACM **15** (1972).
- [10] M. Hansroul et al., Nucl. Inst. and Meth. **A270** (1988) 498.
- [11] I. Gavrilenko, ATL-INDET-97-165 (1997).
- [12] V. Kostyukhin, ATL-PHYS-2003-31 (2003).
- [13] P. Billoir, R. Fruhwirth, M. Regler, Nucl. Inst. and Meth. **A241** (1985) 115.
- [14] P. Billoir, S. Qian, Nucl. Inst. and Meth. **A311** (1992) 139.
- [15] R. Fruhwirth, Nucl. Inst. and Meth. **A262** (1987) 444.
- [16] S. Mehlhase, T. Petersen, CERN-ATL-COM-INDET-2006-017 (2006).
- [17] ATLAS CSC note EG2 - photon identification.

Appendices

A Detector Description - Figures

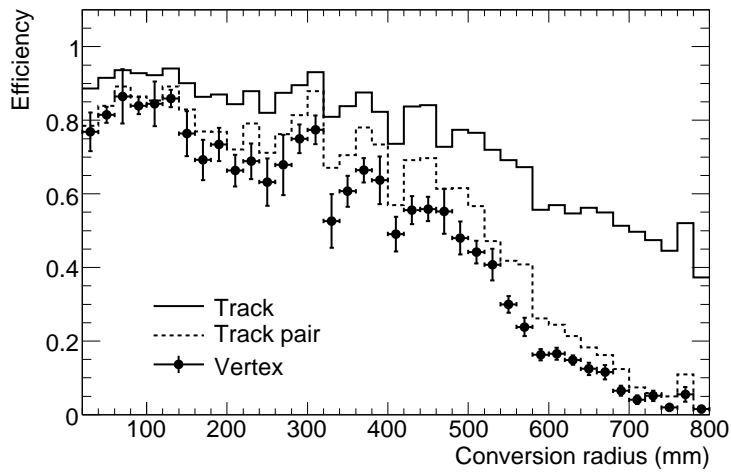


Figure 25: Conversion reconstruction efficiency for conversions coming from 20 GeV p_T photons as a function of conversion radius. The solid histogram shows the track reconstruction efficiency, the dashed histogram shows the track-pair reconstruction efficiency, and the points with error bars show the conversion vertex reconstruction efficiency as shown in the detector paper.

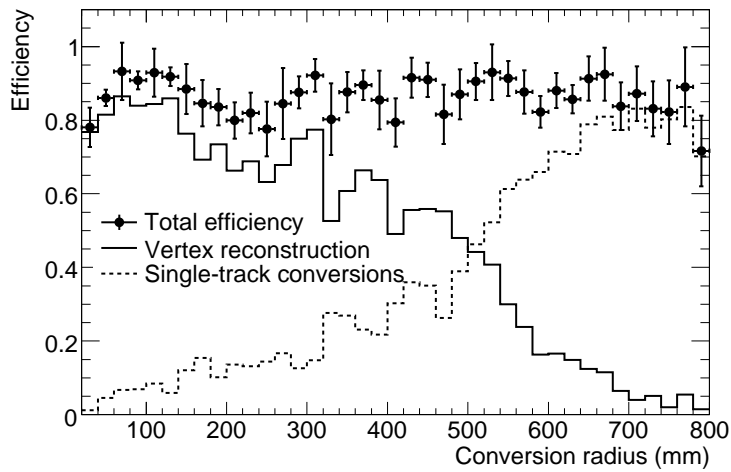


Figure 26: Conversion reconstruction efficiency for conversions coming from 20 GeV p_T photons as a function of conversion radius. The points with error bars show the total reconstruction efficiency, the solid histogram shows the conversion vertex reconstruction efficiency, and the dashed histogram shows the single-track conversion reconstruction efficiency as shown in the detector paper.